Journal of Dentistry 169 (2026) 106623

Contents lists available at ScienceDirect

Journal of Dentistry

journal homepage: www.elsevier.com/locate/jdent

A centripetally rotating implant scan body concept for complete-arch scanning: An in vitro study

Gennaro Ruggiero [a,*], Roberto Sorrentino [a], Fanny Ficuciello [b], Lucio Lo Russo [c], Fariba Esperouz [c], Fernando Zarone [a]

[a] Department of Neurosciences, Reproductive and Odontostomatological Sciences, Division of Prosthodontics, Scientific Unit of Digital Dentistry, University "Federico II" of Naples, Naples, Italy
[b] Department of Electrical Engineering and Information Technology (DIETI), University "Federico II" of Naples, Naples, Italy
[c] Department of Clinical and Experimental Medicine, School of Dentistry, University of Foggia, Foggia, Italy

ARTICLE INFO

Keywords:
Complete-arch
Dental implants
Intraoral scanner
Scan body
Multi-unit abutment
GeoXact
Prosthetic fit

ABSTRACT

Objectives: To assess the in vitro metrological performance of a centripetally rotating implant scan body (ISB) system (GeoXact®), designed to standardize scan-body orientation and create a compact concentric reference geometry to mitigate cumulative stitching drift during complete-arch implant scanning on multi-unit abutments (MUAs), and to investigate site-related effects.

Methods: A maxillary resin cast with four implant sites restored with MUAs was digitized with an industrial optical scanner to generate the reference STL. GeoXact® ISBs were rotated into a centripetal contact configuration to standardize orientation and reduce inter-ISB spacing. Twenty complete-arch scans were acquired with an intraoral scanner (Primescan 2; Dentsply Sirona) by capturing only a partial portion of each ISB head (≥3 planar faces) along the contact chain. Experimental datasets were generated by CAD library replacement. Each dataset was rigidly aligned to the reference using ICP in CloudCompare (global registration). Global mean deviation was computed after global alignment; site-level mean deviations were computed under the same global transformation (no additional per-MUA best-fit), whereas per-MUA rigid alignment was used only to extract translational and angular parameters. Outcomes were global mean deviation, mean deviation per MUA, translational magnitude, angular deviation, Δ interimplant distance, and scanning time.

Results: Global mean deviation was 0.009 ±0.005 mm (n = 20). Mean deviation per MUA was 0.010 ±0.011 mm (n = 80). Translational magnitude and angular deviation averaged 0.064 ±0.092 mm and 0.203 ±0.165°, respectively. Mean Δ interimplant distance was 0.003 ±0.007 mm overall; the distal site showed the largest mean (0.008 ±0.011 mm). Mean scanning time was approximately 9 seconds.

Conclusions: Under controlled in vitro conditions, the tested ISB workflow enabled rapid complete-arch acquisition with small 3D pose deviations on MUAs and limited site-related effects mainly at the distal implant position.

Clinical Significance: In this in vitro model, the GeoXact® centripetal configuration enabled a compact reference geometry and rapid complete-arch acquisition with small metrological deviations.

1. Introduction

Achieving a passive and accurate fit in complete-arch implant-supported prostheses is a fundamental prerequisite for long-term mechanical stability and biological success [1–3]. Framework misfit has been associated with screw loosening, loss of preload, component fracture, marginal bone loss, and increased peri-implant stress, particularly in full-arch restorations where errors accumulate over long spans [4–5]. Consequently, the accuracy of impression techniques remains a central topic in implant prosthodontics, especially for complete-arch rehabilitations.

Accuracy is defined by trueness and precision according to ISO 5725-1, where trueness refers to the closeness of a measurement to the true value and precision describes the repeatability of measurements under

* Corresponding author at: Department of Neurosciences, Reproductive and Odontostomatological Sciences, Division of Prosthodontics, Scientific Unit of Digital Dentistry, University "Federico II" of Naples, 80131, Naples, Italy.
E-mail address: gennaro.ruggiero2@unina.it (G. Ruggiero).

https://doi.org/10.1016/j.jdent.2026.106623
Received 31 January 2026; Received in revised form 6 March 2026; Accepted 9 March 2026
Available online 10 March 2026

identical conditions [6–8]. While intraoral scanners (IOSs) have demonstrated accuracy comparable to conventional impressions for single implants and short-span restorations, their reliability decreases as scan extension increases, particularly in complete-arch implant scenarios [1,9–11]. This reduction in accuracy is primarily related to cumulative stitching errors generated by frame-to-frame alignment algorithms over long edentulous spans [8].

Several in vitro and in vivo investigations have demonstrated that complete-arch IOS accuracy is influenced by multiple interrelated factors, including scan strategy, interimplant distance, implant angulation, scan body geometry, operator experience, and environmental conditions [12–15]. In edentulous arches, the lack of stable anatomical landmarks and the presence of mobile soft tissues further exacerbate stitching-related distortion, particularly at distal implant sites [16–22]. These limitations explain why conventional splinted impressions and high-accuracy extraoral digitization techniques are still widely regarded as reference standards for complete-arch implant restorations [23].

Extraoral photogrammetry has been introduced as a highly accurate digital alternative for recording implant positions in complete-arch rehabilitations [24]. Unlike IOS, photogrammetry systems directly calculate three-dimensional implant coordinates without relying on sequential surface stitching, thereby minimizing cumulative distortion [1,24–26]. Multiple comparative studies and systematic reviews have consistently reported superior trueness and precision for photogrammetry systems when compared with IOS in complete-arch conditions [1, 26]. Additionally, photogrammetry has been associated with reduced scanning time and increased patient and operator satisfaction [27].

Despite these advantages, photogrammetry systems present relevant limitations. They do not capture soft tissue morphology, require an additional impression or scanning step, rely on proprietary hardware and software, and involve high acquisition costs, which restrict their widespread clinical adoption [17,24,28]. Furthermore, environmental factors such as scanning distance and ambient lighting conditions have been shown to influence photogrammetry accuracy, although the magnitude of these effects is generally considered clinically negligible [29–30].

To overcome the limitations of both IOS and extraoral photogrammetry, several alternative and hybrid digital strategies have been proposed. These include splinted implant scan bodies (ISBs), calibrated ISBs, calibrated frameworks, prosthetic-based impression templates, reverse implant scan body techniques, and intraoral photogrammetry systems integrated within IOS platforms [13,19,31–34]. While these approaches generally improve accuracy compared with conventional IOS workflows, they often increase clinical complexity and remain technique-sensitive, and none has yet demonstrated accuracy consistently comparable to extraoral photogrammetry while preserving a simplified chairside workflow [13,34].

Recently, Revilla-León et al. proposed a comprehensive classification of complete-arch implant scanning techniques recorded using IOS, categorizing them into non-splinted ISBs, non-calibrated splinted ISBs, calibrated ISBs, calibrated frameworks, and reverse digitization techniques [33]. This classification highlights that improvements in accuracy are primarily achieved by introducing controlled geometric references, at the cost of additional components and procedural steps [33]. Within the historical evolution of scan-body concepts, improvements in complete-arch IOS accuracy have generally emerged from incremental additions of controlled geometry and spatial constraints. In this context, structured approaches aimed at increasing spatial coherence have been described, including connected/splinted scan-body strategies (e.g., Continuous Scan Strategy, CSS) [35], modular scan-gauge systems that provide controlled overlaps and structured reference geometry (e.g., Nexus IOS®) [36–37], and auxiliary multi-geometry reference aids combined with real-time or library-guided recognition (e.g., Scan Ladder and smart-flag/Apollo concepts) [34,38]. Accordingly, the GeoXact® concept can be positioned as an incremental refinement within this family, differing in implementation by integrating stabilization into a compact centripetal, contact-based orientation mechanism on MUAs intended to concentrate reference geometries and reduce inter-body spacing during acquisition [34–38].

Recent systematic reviews further emphasize the ongoing evolution of scan body concepts and acquisition strategies for complete-arch digital impressions, reinforcing the critical role of ISB geometry and spatial coherence in reducing cumulative distortion [39–40]. These findings support continued research into refined ISB designs aimed at improving interimplant geometric fidelity within IOS workflows.

Collectively, these approaches support the concept that increasing the spatial coherence of reference geometries is a key lever to mitigate cumulative stitching drift across long edentulous spans [34–40]. Building on this conceptual framework, the present hypothesis was that a centripetal contact configuration, by standardizing scan-body orientation, reducing inter-body spacing, and concentrating geometric landmarks, could reduce error propagation during complete-arch acquisition and improve pose registration robustness even with partial head capture.

The aim of this in vitro study was to assess the metrological performance of a patented ISB system featuring a mechanical centripetal rotation/contact mechanism (GeoXact®, Biotec SRL, Vicenza, Italy) for the three-dimensional acquisition of implant position and orientation in complete-arch configurations. Specifically, the study evaluated the global and site-specific mean deviation, translational magnitude, angular deviation, and interimplant distance, as well as the scanning time. Site-related effects were also assessed by testing whether the measured parameters differed among implant positions.

The null hypothesis was that no statistically significant differences would be observed in the tested metrological parameters among the different implant sites when using the tested system.

2. Materials and methods

2.1. Study design

This in vitro study was designed to evaluate the metrological accuracy of a novel patented ISB system (GeoXact®, Biotec SRL, Vicenza, Italy) for registering the three-dimensional position and orientation of implants in a full-arch configuration. The experimental design was based on paired comparisons between experimental datasets and a high-precision metrological reference, using standardized scanning, alignment, and post-processing workflows.

Four implant sites were analysed according to the FDI tooth numbering system, corresponding to positions 1.6, 1.2, 2.2, and 2.6. The choice to analyse a four-implant configuration was intentional and aimed at reproducing a challenging long-span scenario for complete-arch digital acquisition. A reduced number of implants increases interimplant distances, which may amplify cumulative scanning drift; however, clinical configurations with more implants may also introduce additional sources of error (e.g., angulation, depth, access constraints) [1,19,31].

2.2. Tested implant scan body system

The tested ISB system (GeoXact®, Biotec SRL, Vicenza, Italy) consists of centripetally rotating ISBs composed of a fixation body mechanically connected to the MUA, a rotational component allowing controlled angular orientation, and a multi-faceted scanning head with dodecahedral geometry (Fig. 1A-B). This geometry, characterised by multiple edges and vertices, was intentionally selected to enhance the robustness of digital library matching algorithms, enabling accurate spatial registration even when only a partial portion of the ISB head is acquired.

A defining feature of the tested ISB system is the centripetal rotation mechanism, which allows the ISB heads to be oriented toward the center of the arch until mutual contact is achieved (Fig. 1C). This configuration

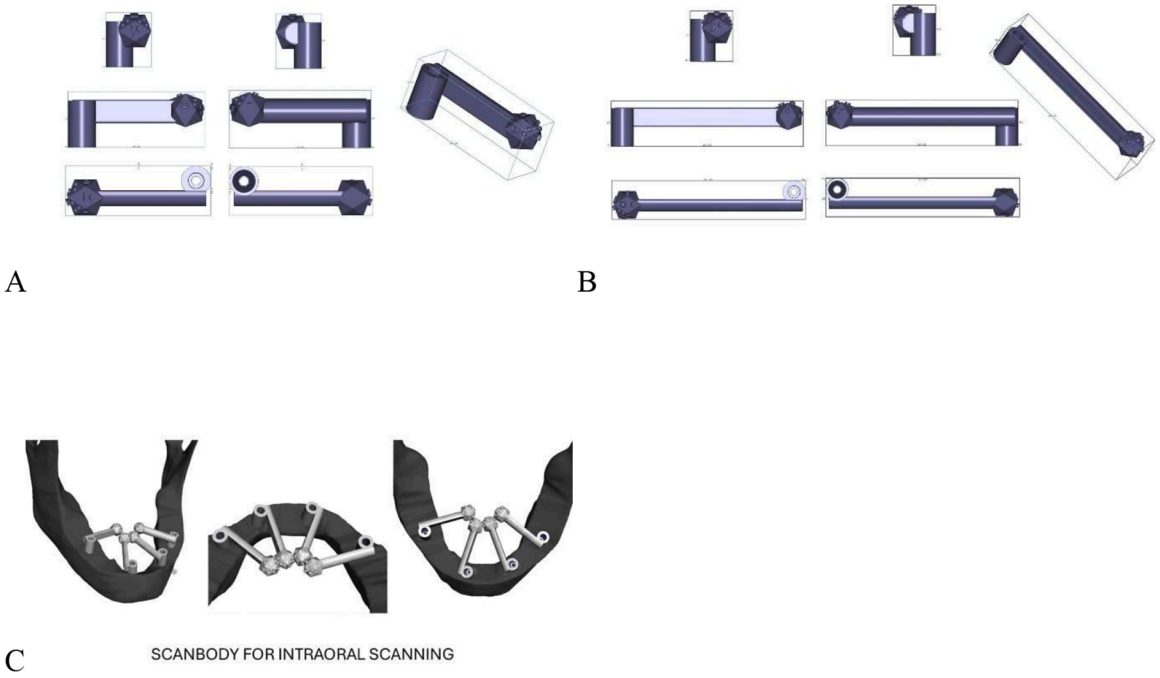

Fig. 1. Technical drawings and instructions for use. A, technical drawings of GeoXact with a 2 cm arm; B, GeoXact with a 4 cm arm; C, centripetal rotation of the heads until they contact.

standardises ISB orientation across implants, produces a compact and concentric arrangement of reference geometries, reduces the overall scanned volume, and limits optical noise and cumulative stitching errors. Additionally, solid geometry facilitates the closure of vertical gaps between implants placed at different heights (Figs. 1B-C), further improving the consistency of the acquisition geometry.

All ISBs were manufactured from medical-grade titanium alloy (Ti-^{6}Al-^{4}V, Grade 5), a material commonly used for implant abutments due to its high dimensional stability and favourable optical properties for intraoral scanning. The investigated ISBs were pre-commercial prototypes provided as manufactured with a matte, roughened surface finish to reduce specular reflections and facilitate optical scanning; this finish is consistent with a post-print relaxation (stress-relief) followed by light abrasive blasting.

2.3. Master cast

A patient-derived virtual cast representing a maxillary arch was used as the digital source geometry for model fabrication. The model included four implants positioned at 1.6, 1.2, 2.2, and 2.6. The virtual cast was additively manufactured as a physical model using a photopolymer resin specifically formulated for dental models (Liqcreate Dental Model Pro Grey, Liqcreate, Leiderdorp, Netherlands), selected for its dimensional stability, low polymerization shrinkage, and suitability for implant analog placement. The printing process was performed using a dedicated 3D printer (NexDent LCD1, 3D Systems, Soesterberg, Netherlands).

After fabrication, digital implant analogs were inserted into the printed cast, and compatible multi-unit abutments were connected to each analog according to the manufacturer's specifications. This physical model constituted the master cast used for both reference and experimental acquisitions.

2.4. Reference dataset

A high-accuracy reference virtual cast was made using an industrial structured-light metrological scanner (Atos Core 80, GOM-ZEISS, Braunschweig, Germany), with a working distance of 170 mm, a point spacing of 0.03 mm, and a measurement accuracy of ±0.0025 mm [20–21]. The resulting reference dataset was exported into Standard Tessellation Language (STL) file format in mm.

The reference STL dataset was imported into a dedicated software program (DentalCad v. 6.2, EGSolutions, Bologna, Italy). Within this environment, the digital libraries of the corresponding ISB MUAs were aligned to the reference scan. The resulting aligned dataset constituted the reference virtual cast against which all experimental datasets were compared.

2.5. Experimental scanning protocol

Following reference acquisition, the tested ISBs were screwed at 5 Ncm onto 4 digital analog MUAs (GeoXact® MUA-digital analog, Biotec SRL, Vicenza, Italy) mounted on the master cast. Each ISB was then rotated around its longitudinal axis using the centripetal rotation feature, so that the ISB heads were oriented toward the center of the arch until physical contact between adjacent heads occurred (Fig. 2B). This centripetal contact configuration was consistently adopted for all experimental scans to standardize orientation and spatial relationships among ISBs.

For each ISB, only a partial portion of the scanning head was acquired. Specifically, at least three planar faces of the dodecahedral geometry were scanned for each ISB head. This limited acquisition strategy was intentionally adopted to reduce scanning time and data redundancy while testing whether reliable spatial registration could be achieved from partial surface information alone. This partial-capture protocol was adopted to test whether pose registration could remain stable under reduced surface information in a controlled setting. Clinical reproducibility of partial capture, particularly for less experienced operators and under intraoral conditions, has not been established. The scan was made sequentially starting from MUA 2.2, followed by 1.2, 1.6, and finally 2.6. This order was chosen to follow the continuous chain of physical contact between adjacent MUA heads, ensuring consistent overlap and preventing unscanned gaps during data acquisition. A total of 20 experimental scans were analyzed. For each scan, four MUA positions were

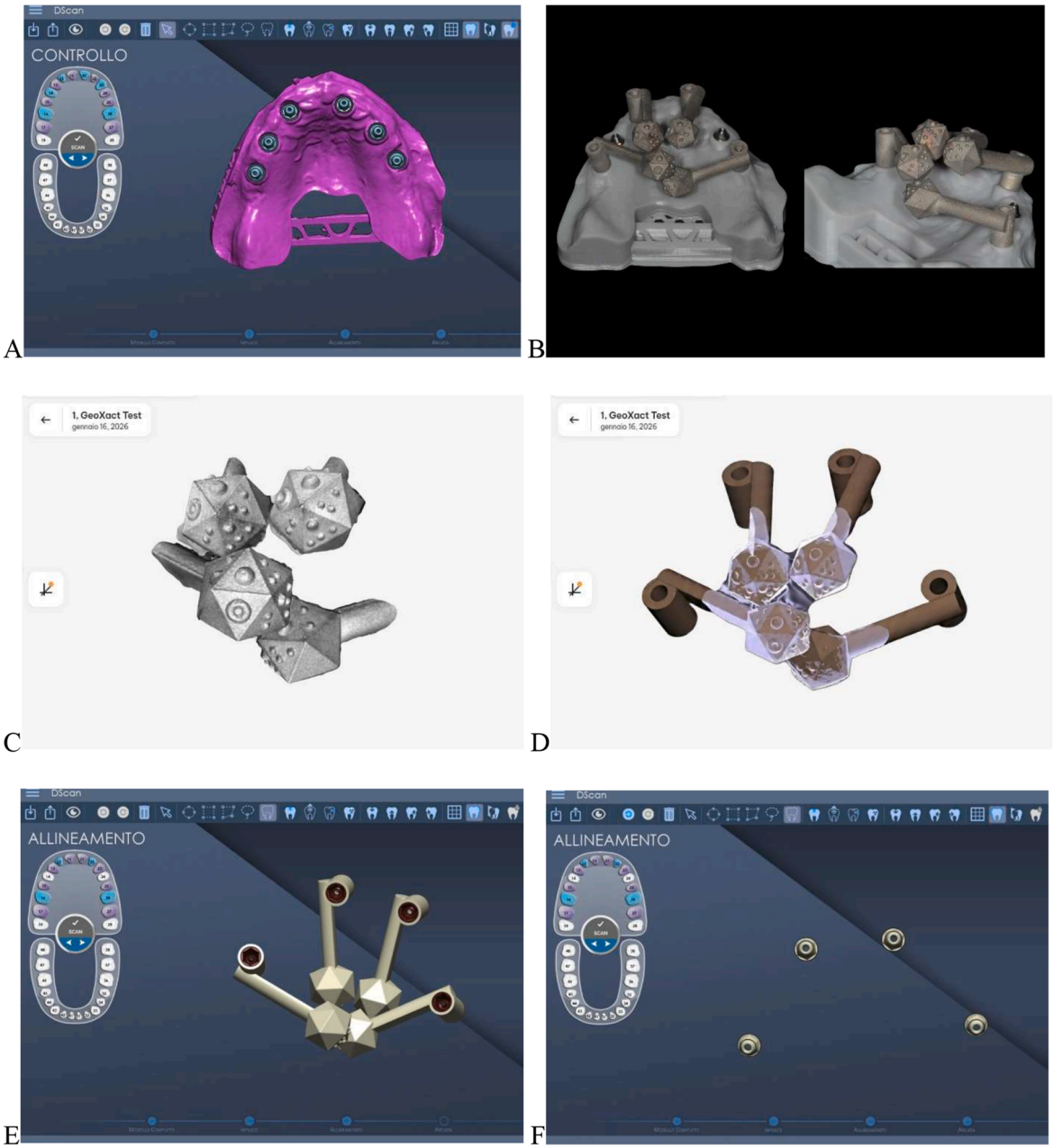

Fig. 2. Study design. A, Reference Scan; B, GeoXact screwed on the typodont. C, Scan made with an intraoral scanner (IOS) on only a part of the head; D, Alignment of the CAD library data to the scan made with IOS; E, MUA alignment from the library; F, MUA segmentation.

evaluated (1.6, 1.2, 2.2, 2.6), yielding 80 single-site observations (20 scans × 4 sites). No spray or powder was used on the ISBs.

2.6. Intraoral scanner acquisition

All experimental scans were acquired using an IOS (Primescan 2, SW 5.3.3; Dentsply Sirona Inc, Bensheim, Germany) (Fig. 2C).

The scans were performed by an expert in digital dentistry and prosthodontics (X.X.). Prior to data acquisition, the IOS was calibrated according to the manufacturer's indication and the operator underwent a structured training and calibration phase consisting of 10 repeated trial scans of the same configuration until consistent scan quality, reproducible surface coverage, stable scan times, and homogeneous mesh density were achieved [41].

Scanning was conducted under controlled laboratory conditions in a single session. Ambient temperature was maintained at approximately 22°C, relative humidity was kept within the range of 45-55 %, and diffuse ambient lighting at 10,000 lux, according to previous studies [30], with a daylight-like color temperature of approximately 5,500 K to reduce specular reflections on the ISBs' surfaces. All scans were performed using a continuous scanning strategy, and the total scanning time required to acquire the 4 ISB heads was recorded for each experimental scan. Scan order randomization was not considered necessary because the same fixed master cast configuration was repeatedly acquired to characterize the system's metrological performance.

2.7. Generation of experimental datasets

Each IOS acquisition was imported into the DentalCad software program. Within the software environment, the corresponding ISBs were matched to the scanned ISB head geometries (Fig. 2D) and the corresponding MUAs were selected (Fig. 2E). This process generated twenty

experimental STL datasets in mm, each containing four MUAs positioned in space according to the spatial information captured by the IOS (Fig. 2F). Since the final experimental STL datasets were produced through library matching (CAD replacement of the ISB/MUA geometry), the metrological assessment mainly quantifies the accuracy of the recorded spatial pose (position and orientation) as determined by the IOS acquisition and the matching algorithm, rather than the surface-mesh fidelity of the scanned component. For this reason, mesh-reconstruction errors affecting the MUA geometry are intentionally reduced by the adopted workflow, whereas potential inaccuracies related to image acquisition, stitching, ISB capture and library matching remain incorporated in the resulting pose.

2.8. Metrological evaluation workflow

All metrological analyses were performed using CloudCompare (version 2.14, Girardeau-Montaut, Télécom Paris Tech/EDF R&D, GPL license), a software program for three-dimensional point cloud and mesh processing.

Fine registration was performed using CloudCompare's ICP (rigid) algorithm with 6 degrees of freedom (rotation + translation; no scaling). ICP was run using the software's default convergence settings (stopping when the mean deviation decrease between 2 consecutive iterations fell below 1×10^{-5}, or after a maximum of 20 iterations) and the default random sampling limit of 50,000 points per iteration. No additional transformation constraints were applied (no axis-locking), and farthest-point removal/outlier rejection was not enabled (default setting). Registration was computed using the entire MUA surface as the alignment region.

The analytical workflow followed established CloudCompare procedures for rigid registration and surface distance computation in mm and degrees, in line with previously described methodologies [16,18,34,42] (Fig. 3). The overall approach aligns with ISO 20896-1 principles for assessing digital impression accuracy, by comparing a device-generated dataset against a metrological reference under controlled conditions and quantifying deviations through rigid registration and distance-based

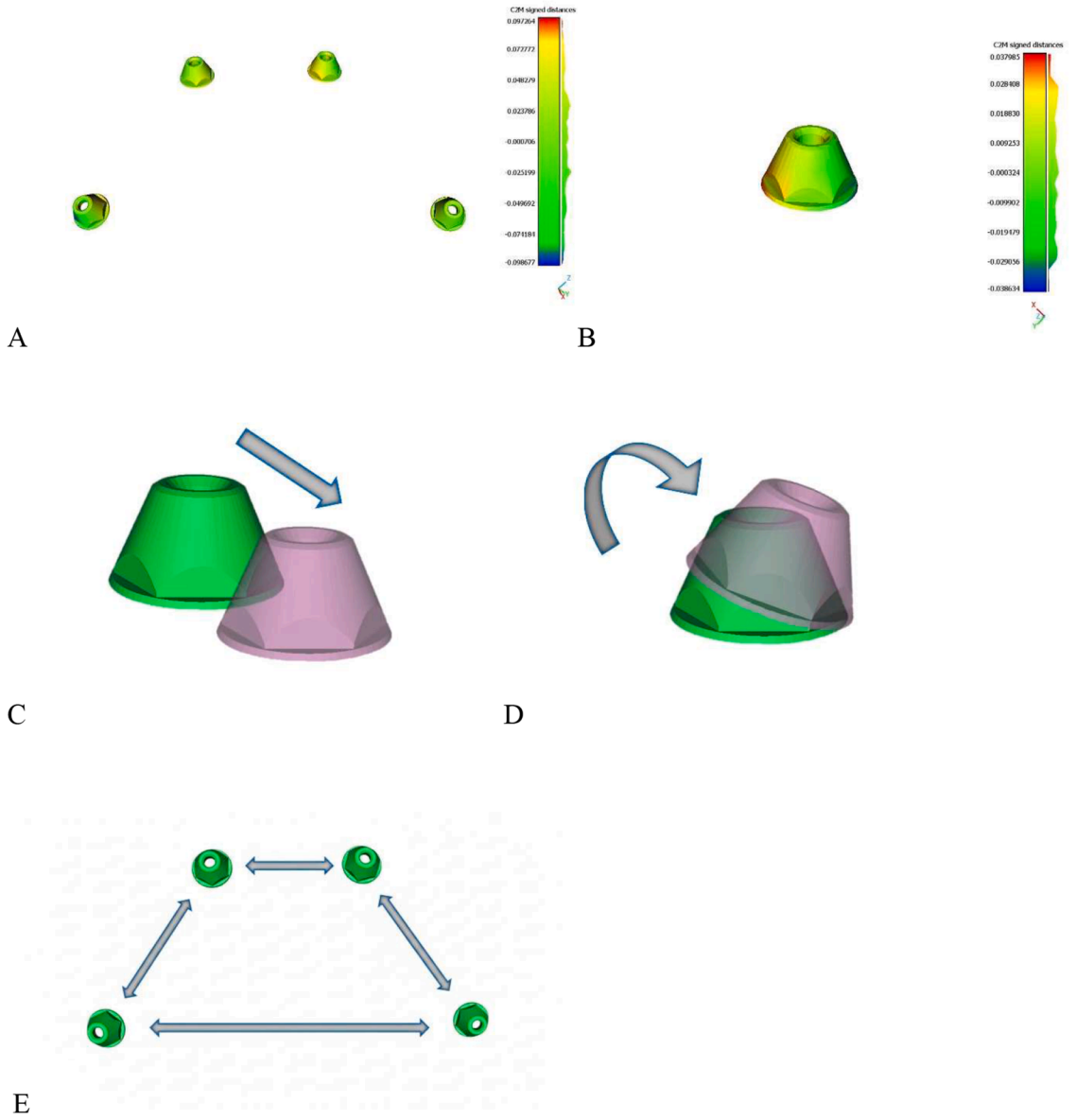

Fig. 3. Metrological analysis of experimental and reference data. Color-scale limits were set for visualization only (deviations were well below 150 μm), and the small lateral undulations next to the color bar represent the distance histogram. A, Mean deviation of the whole Multi-unit abutments (MUAs) surface data from the reference in mm; B, Mean deviation between single experimental MUAs and reference in mm. C, Translational magnitude. D, Angular deviation. E, Interim-plant distance.

metrics (trueness-oriented evaluation) [7].

The analysis was conducted in two stages. First, each experimental full-arch dataset was globally registered to the reference to align the entire multi-MUA configuration; global mean deviation was then computed as the residual mean surface distance between the reference and experimental datasets. Second, each MUA was segmented from both reference and experimental datasets and analyzed independently: (i) single-MUA mean deviation was computed on each segmented MUA under the fixed global transformation (no additional per-MUA best-fit); (ii) inter-implant distances were computed on the segmented MUAs; (iii) translation and rotation were extracted from the rigid transformation matrix of the segmented MUA-to-reference MUA alignment (axis-specific translation components Tx, Ty, Tz; translational magnitude ‖t‖; and angular deviation). MUA-level rigid alignment was used only to extract translation and rotation parameters from the matrix resulting from this alignment.

2.8.1. Global mean deviation analysis

For each experimental dataset, a rigid registration was first performed between the experimental STL and the reference STL (Fig. 3A) [19,31]. The global geometric discrepancy was quantified using the mean deviation, calculated as

$$\text{Mean deviation} = \frac{1}{N}\sum_{i=1}^{N} d_i$$

where $d_i$represents the absolute residual distance between corresponding surface points and $N$is the number of evaluated points. Mean deviation was selected because it provides a single synthetic measure of the overall agreement between datasets and is widely used in metrological assessments of geometric accuracy.

2.8.2. Single-MUA mean deviation analysis

To evaluate site-specific surface discrepancy, each of the four MUAs was segmented individually from the experimental datasets [34]. Mean deviation was then calculated separately for each segmented MUA using the same definition adopted for the global analysis (absolute point-to-surface residuals averaged across the evaluated points) (Fig. 3B). This approach allowed assessment of local deviations without the masking effect of global averaging across the entire implant assembly.

Importantly, single-MUA mean deviation was computed without any additional MUA-level re-registration. After the initial global rigid registration of each experimental dataset to the reference, the resulting transformation matrix was kept fixed and applied to the segmented MUAs. Mean deviation was then calculated on each segmented MUA under the same global transformation, so that local values reflected residual site-specific discrepancies rather than an artefactual “best-fit” of each individual component.

2.8.3. Translational components and translational magnitude

Rigid registration in CloudCompare yields a translation vector $\mathrm{t} = (T_x, T_y, T_z)$. The translation components (Tx, Ty, Tz) were expressed in the Cartesian coordinate system of the reference dataset (reference virtual cast), which acted as the master coordinate frame for all registrations. Therefore, axis directions are dataset-defined (not anatomy-defined); for this reason, directionality was interpreted conservatively and, when needed, analyses were performed on absolute axis components and on detrended values to minimize scan-level rigid-body effects. Translational deviation was expressed as the Euclidean norm of this vector, defined as

$$\left|T\right| = \sqrt{T_x^2 + T_y^2 + T_z^2}$$

This scalar quantity was selected because it provides a direction-independent measure of translational displacement, enabling straightforward comparison between scans (Fig. 3C).

To isolate object-specific translation, a detrending procedure was applied. For each scan, the mean translation vector across the four MUAs was calculated as

$$\bar{\mathrm{t}} = \frac{1}{4}\sum_{j\in\{A,B,C,D\}} \mathrm{t}_j$$

The detrended translation vector for each MUA was then obtained as

$$\mathrm{t}_j^* = \mathrm{t}_j - \bar{\mathrm{t}}$$

and its magnitude computed as

$$\left|T_j^*\right| = \| \mathrm{t}_j^* \|$$

This detrending removes scan-level rigid translation and isolates the relative translational behaviour of each MUA within the scan. Because detrended values retain directional information, absolute magnitudes were used for statistical analyses.

2.8.4. Angular deviation and detrending

Angular deviation was defined as the residual rotational discrepancy between experimental and reference MUAs after rigid alignment (Fig. 3D). To remove scan-level rotational components affecting all MUAs similarly, angular deviation was detrended by subtracting the mean angular deviation of the four MUAs within each scan. The mean angular deviation was computed as

$$\bar{\theta} = \frac{1}{4}\sum_{j\in\{A,B,C,D\}} \theta_j$$

and the detrended angular deviation for each MUA was defined as

$$\theta_j^* = \theta_j - \bar{\theta}$$

Absolute values $\left|\theta_j^*\right|$were used for statistical inference to quantify the magnitude of object-specific rotational deviation independent of direction.

2.8.5. Interimplant distance analysis

Interimplant spatial relationships were evaluated using a surface-based approach rather than centroid-based metrics. Because MUAs exhibit quasi-conical geometries, clinically relevant misfit may manifest as localized surface discrepancies. For this reason, interimplant distances were assessed by computing point-to-surface distances between experimental and reference MUA surfaces (Fig. 3E). For a given experimental surface point p, the distance to the reference surface $S_{ref}$was defined as

$$d(\mathrm{p}, S_{ref}) = \min_{\mathrm{q}\in S_{ref}} \| \mathrm{p} - \mathrm{q} \|$$

Within a predefined region of interest (ROI) on the MUA surface, two summary metrics were retained: the maximum surface deviation (Max Error) and the standard deviation of the distance distribution (σ). The ROI was defined on the external lateral surface of each MUA, excluding (i) any non-clinical internal surfaces, and (ii) sharp marginal edges or small planar facets that may amplify discretization artefacts in point-to-surface distance computation. To ensure comparability of Max Error and σ across all sites and scans, the ROI was defined once on the reference CAD-derived MUA mesh and saved as a fixed subset of surface elements (triangles/vertices) on the external lateral surface. Because all experimental MUAs were generated by library matching (CAD replacement), the same CAD geometry (and mesh topology) was used in every experimental dataset; therefore, the identical ROI subset could be propagated unchanged to each corresponding MUA in every scan, without per-scan or per-site re-definition. All point-to-surface distances were then

computed exclusively within this fixed ROI. Mean distances and centroid-to-centroid measurements were intentionally avoided because they may obscure higher-end (upper-percentile) deviations and are sensitive to surface sampling density.

Delta values were calculated by subtracting reference values from experimental values according to

$$\Delta MaxError = MaxError_{exp} - MaxError_{ref}$$

and

$$\Delta\sigma = \sigma_{exp} - \sigma_{ref}$$

Positive delta values indicate increased local deviation compared with the reference configuration.

2.9. Statistical analysis

Statistical analysis followed a repeated-measures design, as each scan contributed measurements for all four implant sites by using a dedicated software program (SPSS v25, IBM Corp., Armonk, NY, USA). Descriptive statistics were calculated for each variable overall and per site, including sample size, mean, standard deviation, median, interquartile range, and minimum-maximum values. Data normality was assessed using the Shapiro-Wilk test. In addition to normality testing, homogeneity of variances across implant sites was assessed using Levene's test.

For between-site comparisons of detrended translational magnitude, detrended angular deviation, and single-MUA mean deviation, repeated-measures analysis of variance was applied when normality assumptions were met for all sites; otherwise, the Friedman test was used. Post-hoc comparisons were conducted using paired tests, either paired t-tests or Wilcoxon signed-rank tests, with Holm correction applied to control for multiple comparisons. Post-hoc pairwise comparisons were performed only when the omnibus test was statistically significant.

Delta metrics (Δ interimplant distance and Δσ) were tested against zero at the site level only (n = 20 per site; one observation per scan), to avoid pseudo-replication due to within-scan repeated measures across the four implant sites. Accordingly, no pooled one-sample tests treating all sites as independent observations (n = 80) were performed. The choice between parametric and non-parametric one-sample tests was based on normality (Shapiro-Wilk) within each site. Effect sizes were reported as partial eta squared for repeated-measures ANOVA, Kendall's W for Friedman tests, Cohen's d for parametric paired comparisons, and r for non-parametric tests. Statistical significance was set at $\alpha = 0.05$.

An a priori sample size calculation was performed using G*Power (v3.1.9.7; Heinrich Heine University Düsseldorf, Germany). A repeated-measures within-subject ANOVA model was used as an approximation of the planned non-parametric repeated-measures analysis. With $\alpha = 0.05$, power $(1-\beta) = 0.95$, and an expected moderate effect (Kendall's W = 0.30), the required sample size was n = 20. This effect size was selected based on previous metrological studies in implant prosthodontics and on the expected magnitude of site-related deviations in full-arch workflows [30].

Therefore, the number of experimental scans included in the present study was considered sufficient to support the primary statistical analyses and the interpretation of site-related differences.

3. Results

Normality testing (Shapiro-Wilk) indicated non-normal distributions for the main accuracy variables across sites; therefore, non-parametric repeated-measures statistics (Friedman) were used for site comparisons, followed by pairwise Wilcoxon signed-rank tests with Holm correction for multiple comparisons. Levene's test showed no consistent evidence of variance homogeneity across implant sites, supporting the use of non-parametric repeated-measures statistics.

3.1. Scanning time

The mean scanning time required to acquire the four ISB heads was 9.0 ±1.8 seconds per scan, confirming the rapid acquisition enabled by the centripetal configuration and the reduced scanned surface area (Supplemental Video 1).

3.2. Global mean deviation

The global mean deviation (4 MUAs together versus reference) (Fig. 3A) across the 20 scans showed a mean ± SD of 0.009 ±0.005 mm, with median 0.008 (IQR 0.006-0.012) and a range of 0.001-0.024 mm (n = 20) (Table 1).

3.3. Mean deviation per single MUA by site

A statistically significant overall difference across sites was detected for single-MUA mean deviation (Friedman $\chi^2(3) = 14.879$, $p = 0.002$, Kendall's $W = 0.248$). Post-hoc (Holm-corrected) Wilcoxon signed-rank tests identified higher mean deviation at site 1.2 compared with sites 2.6 ($p\_adj < 0.001$, $r = 0.810$) and 1.6 ($p\_adj = 0.0136$, $r = 0.643$). Other pairwise comparisons were not significant after correction.

Overall, mean deviation per MUA was 0.010 ±0.011 mm (median 0.006; n = 80). Descriptive statistics are reported in Tables 1-2 and Fig. 4A. The distribution of site-specific mean deviation values, including data density and individual observations, is shown in Fig. 5A.

3.4. Translational deviation

Translational magnitude differed among the four implant sites (Friedman $\chi^2(3) = 9.154$, $p = 0.027$, Kendall's $W = 0.153$), indicating a small-to-moderate site effect.

Post-hoc (Holm-corrected) comparisons identified a significant difference only between sites 2.2 vs 2.6: $p\_adj = 0.015$, Wilcoxon $r = 0.672$. All other pairwise comparisons were not significant after Holm correction. Descriptive statistics were reported in Tables 1-2 and Fig. 4B. Raincloud-like violin plots further illustrate the distribution of detrended translational magnitude across sites (Fig. 5B).

3.5. Angular deviation

The overall site effect for angular deviation did not reach conventional statistical significance (Friedman $\chi^2(3) = 7.129$, $p = 0.067$, Kendall's $W = 0.119$). Descriptive statistics were reported in Tables 1-2 and Fig. 4C. The distribution of detrended angular deviation by site is reported in Fig. 5C. As the omnibus Friedman test did not reach statistical significance ($p = 0.067$), no confirmatory post-hoc pairwise comparisons were performed for angular deviation.

3.6. Delta metrics versus reference (bias testing against zero)

3.6.1. Δ Interimplant distance from reference

Site-level one-sample testing (n = 20 per site) showed that Δ interimplant distance differed from zero only at site 2.6 (mean 0.008 mm; $W = 1.0$, $p = 0.004$, $r = 0.64$). The remaining sites did not show statistically significant one-sample deviations from zero after normality-based test selection. Descriptive statistics are reported in Tables 1-2 and Fig. 4D.

3.6.2. Δ Sigma from reference

Site-level one-sample testing (n = 20 per site) identified significant deviations from zero for Δσ at site 1.2 (mean -0.001 mm; $W = 20.0$, $p < 0.001$, $r = 0.757$), site 1.6 (mean -0.001 mm; $W = 32.5$, $p = 0.029$, $r = 0.486$), and site 2.2 (mean -0.002 mm; $t(19) = -2.523$, $p = 0.02$, Cohen's $d = -0.564$). Site 2.6 did not show a statistically significant one-sample deviation for Δσ at $\alpha = 0.05$.

Table 1
Overall descriptive statistics (in mm; mean ± SD, median, Interquartile range, min-max) for all primary metrics.

Metric	N	Mean	SD	Median	Q1	Q3	Min	Max
Global mean deviation	20	0.009	0.005	0.008	0.006	0.012	0.001	0.024
Mean deviation per MUA	80	0.010	0.011	0.007	0.002	0.016	0.0001	0.042
Translational Magnitude	80	0.064	0.092	0.033	0.011	0.086	0.0	0.58
Angular deviation (degree)	80	0.203	0.165	0.171	0.096	0.293	0.003	0.93
Δ Interimplant distance	80	0.003	0.007	0.0	-0.001	0.006	-0.005	0.036
Δ Sigma from Reference	80	-0.001	0.006	-0.001	-0.003	0.0	-0.043	0.035

Global mean deviation is reported per scan (n = 20). For MUA-level metrics (single-MUA mean deviation, translational magnitude, angular deviation, Δ interimplant distance, and Δσ), overall descriptive statistics are reported across all observations (n = 80 = 20 scans × 4 sites). One-sample inference for Δ metrics was performed at the site level only (n = 20 per site), not on pooled data. SD, standard deviation; Q1, 1st quartile; Q3, 3rd quartile.

Table 2
Site-wise descriptive statistics. Descriptive statistics in mm (n = 20; mean ±SD, median, IQR, min-max) for all primary metrics by anatomical site (sites 1.6, 1.2, 2.2, 2.6).

Metric	Site	Mean	SD	Median	Q1	Q3	Min	Max
Translational Magnitude	1.2	0.054	0.053	0.031	0.016	0.094	0.0	0.18
	1.6	0.040	0.032	0.03	0.018	0.057	0.0	0.14
	2.2	0.051	0.081	0.021	0.003	0.054	0.0	0.34
	2.6	0.112	0.146	0.066	0.02	0.143	0.0	0.58
Angular Deviation (degree)	1.2	0.196	0.142	0.17	0.1	0.267	0.003	0.502
	1.6	0.122	0.068	0.116	0.079	0.176	0.005	0.26
	2.2	0.268	0.207	0.2425	0.131	0.351	0.003	0.93
	2.6	0.224	0.185	0.185	0.113	0.315	0.003	0.7
Mean deviation per MUA	1.2	0.017	0.013	0.016	0.007	0.019	0.0004	0.042
	1.6	0.006	0.005	0.006	0.001	0.009	0.0001	0.016
	2.2	0.013	0.012	0.008	0.004	0.019	0.0002	0.042
	2.6	0.006	0.010	0.002	0.001	0.006	0.0001	0.035
Δ Interimplant distance	1.2	0.001	0.002	0.0	-0.001	0.003	-0.003	0.007
	1.6	0.001	0.004	0.0	-0.001	0.004	-0.004	0.009
	2.2	0.001	0.005	0.0	-0.001	0.001	-0.005	0.017
	2.6	0.008	0.011	0.003	0.0	0.013	-0.001	0.036
Δ Sigma from Reference	1.2	-0.001	0.008	-0.003	-0.005	-0.002	-0.007	0.035
	1.6	-0.001	0.001	-0.001	-0.001	0.0	-0.006	0.001
	2.2	-0.001	0.002	-0.001	-0.003	0.0	-0.008	0.003
	2.6	-0.002	0.01	0.0	-0.003	0.002	-0.043	0.006

3.7. Directionality of translational error (|Tx|, |Ty|, |Tz|)

Within each site, comparisons of the absolute axis components did not show evidence of a consistent directional dominance: Site 1.2: Friedman p = 0.137; Site 1.6: Friedman p = 0.186; Site 2.2: Friedman p = 0.086; Site 2.6: Friedman p = 0.368.

Accordingly, no Holm-corrected post-hoc contrasts between |Tx|, |Ty|, and |Tz| reached significance, suggesting that translation errors were not strongly anisotropic within the analyzed coordinate system. Directional behaviour was additionally explored visually using translational vector plots and bivariate scatter plots of absolute axis components (Fig. 6), confirming the absence of dominant directional trends.

4. Discussion

The present in vitro study evaluated the metrological performance of a centripetally rotating ISB system (GeoXact®) for complete-arch implant position registration, showing a reliable three-dimensional approach with limited site-related variability.

Low residual surface discrepancies were observed versus the reference, with a global mean deviation of 0.009 ±0.005 mm and an overall single-MUA mean deviation of 0.010 ±0.011 mm. These values are comparable with an in-vitro, real-time library-matching workflow reporting a pooled mean deviation of 0.013 ±0.009 mm and higher deviations at posterior positions (up to 0.026 ±0.008 mm) [34]. In systematic evidence, in-vitro complete-arch workflows report mean surface deviations of 0.014–0.067 mm for IOS and 0.005–0.048 mm for stereophotogrammetry, with corresponding angular deviation ranges of 0.28°–1.177° (IOS) and 0.24°–0.81° (stereophotogrammetry) [1]. In the present study, Δ interimplant distance was 0.003 ±0.007 mm overall (n = 80), with the largest site-specific mean at the distal position (site 2.6) of 0.008 ±0.011 mm (n = 20), while mean angular deviation was 0.203 ±0.165° (n = 80). Under optimal acquisition conditions, a photogrammetry distance study reported mean linear and angular discrepancies of 0.017 ±0.004 mm and 0.17 ±0.02°, supporting the reduced cumulative distortion expected when sequential stitching is avoided [29]. As regards 3D displacement, in the present study, detrended translational magnitude averaged 0.064 ±0.092 mm. Using different terminology, an in vitro study reported 3D Euclidean deviations at the ISB-MUA level of approximately 0.093-0.121 mm depending on scan body type and 0.085-0.135 mm depending on the IOS [13]. Direct numerical comparisons should nevertheless be interpreted cautiously because reference standards, devices, scan body designs/materials, alignment parameters, ROI definitions, and outcome formulations are not directly comparable across studies [1,13,19,29,34].

Importantly, clinical literature indicates that direct intraoral scanning can be clinically feasible for full-arch implant prostheses when performed by experienced operators and when supportive strategies are implemented [1,24,36,39,40].

Mean angular deviations remained below 1°, and mean linear discrepancies were below 0.150 mm (Table 1), values that are commonly reported in the literature but are not universally accepted as definitive passive-fit thresholds, as clinical acceptability depends on framework material, manufacturing tolerances, prosthetic design, and verification procedures [1,39–40]. Site-related differences were mainly driven by the distal position (2.6), which showed slightly higher translational discrepancies and the only statistically detectable inter-implant distance bias. This pattern is consistent with less favourable posterior access/line-of-sight and with minor error propagation along the continuous scanning chain (stitching/registration drift) toward the

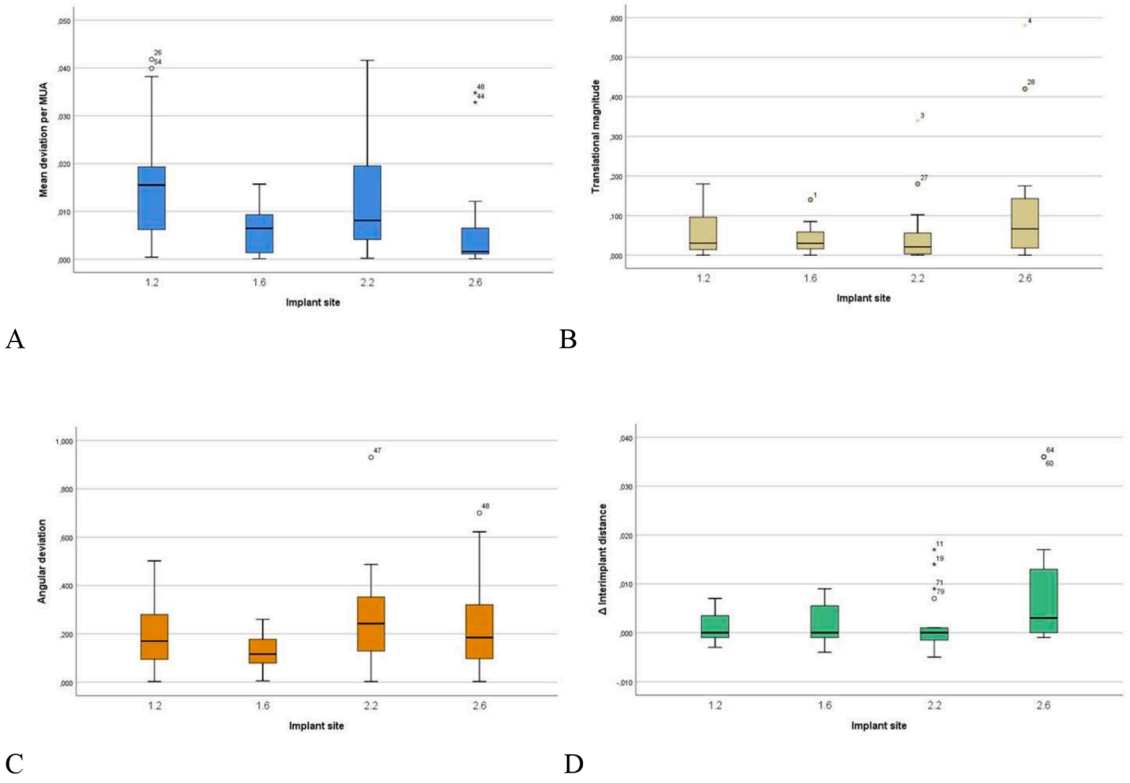

Fig. 4. Box-and-whisker plot illustrating metrological values. Sites are shown in FDI notation. The box extends from the first to the third quartile, while the upper and lower whiskers indicate the minimum and maximum values. The line within the box represents the median, and open circles denote potential outliers. A, Mean deviation per single MUA in mm; B, Translational magnitude in mm; C, Angular deviation in degree; D, Δ Interimplant distance in mm.

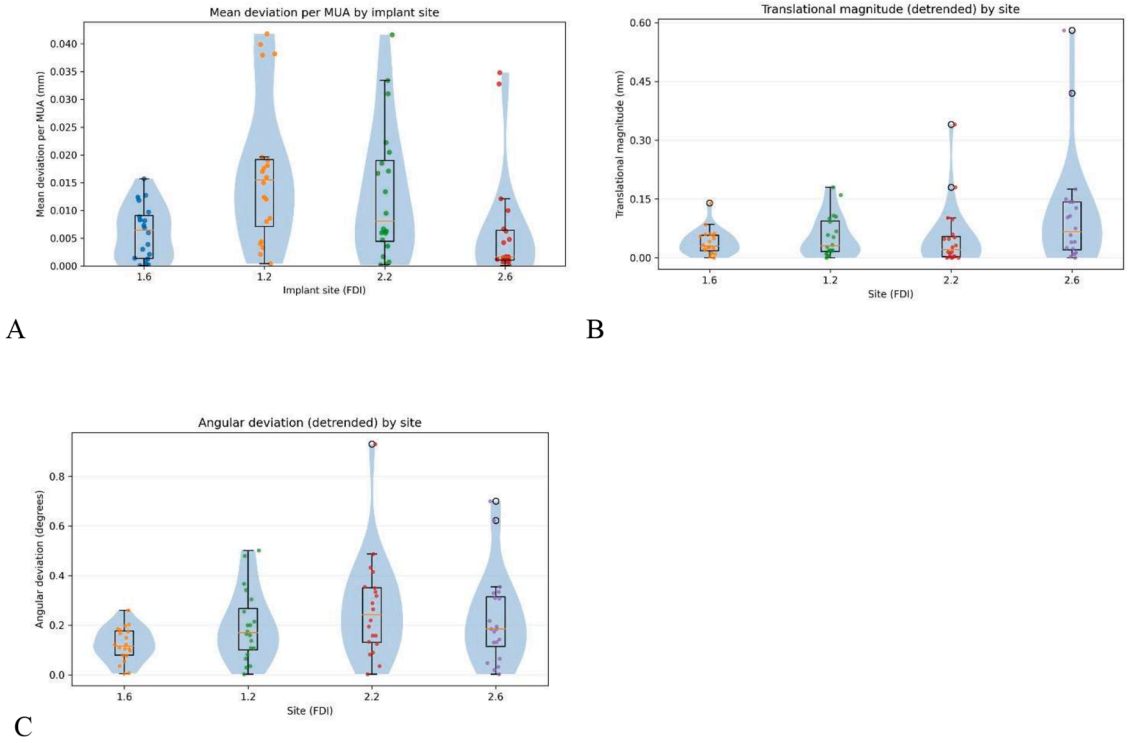

Fig. 5. Distribution of site-specific metrological outcomes (raincloud-like violin plots). A, Raincloud-like violin plot (violin with overlaid boxplot and jittered individual observations) showing single-MUA mean deviation by implant site in mm. B, Raincloud-like violin plot of detrended translational magnitude by site in mm. C, Raincloud-like violin plot of detrended angular deviation by site. For each panel, the violin width represents data density; the box indicates median and interquartile range; whiskers/outliers follow standard boxplot conventions; dots represent individual scan-level observations ($n = 20$ per site).

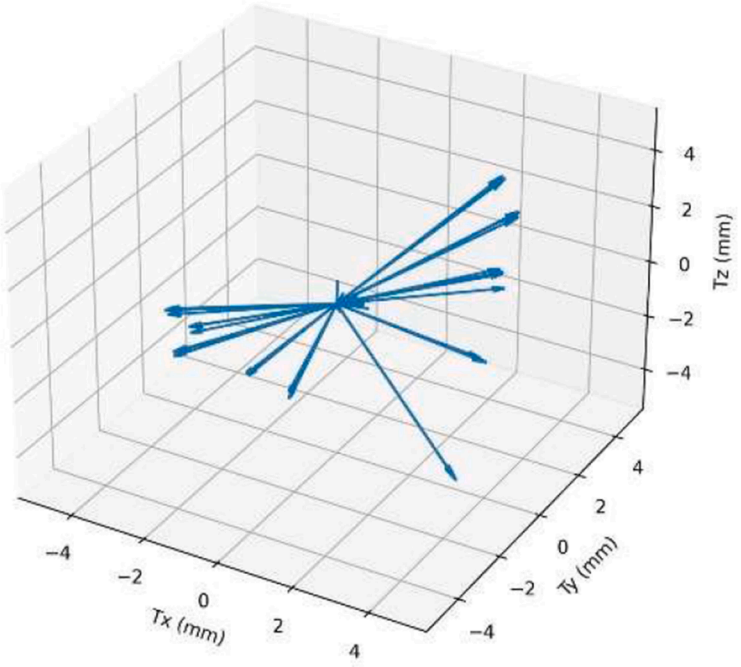

Fig. 6. Directionality assessment of translational error (Tx, Ty, Tz) in mm. Three-dimensional quiver plot representing the translational vectors (Tx, Ty, Tz) obtained from rigid registration for all observations (20 scans × 4 sites), displayed from a common origin to visualize overall dispersion and absence of directional clustering.

terminal segment, and aligns with previous evidence indicating distal positions as more error-prone in complete-arch acquisitions [13,34,43–44]. In the present study, this did not translate into a preferential translational direction, in agreement with the absence of significant anisotropy among translational components, and angular deviation showed no significant overall site effect. Conversely, the higher single-MUA mean deviation observed at 1.2 likely reflects a local surface/acquisition effect (partial coverage, viewing-angle and overlap variability) rather than a clinically meaningful deterioration, as it was not mirrored by a consistent site effect on angular outcomes. Although some site-related differences reached statistical significance, the absolute magnitudes were small, and the present metrological endpoints cannot determine whether such differences would translate into clinically detectable misfit; correlation with verification indices and framework fit outcomes remains necessary.

A methodological strength is the use of detrended translational and angular metrics, which reduce scan-level rigid-body effects that can mask implant-specific behaviour when only global best-fit alignment is considered [1,13]. In addition, the surface-based interimplant evaluation adopted in this study improves clinical interpretability compared with centroid-based approaches, as it quantifies deviations across the entire MUA surface rather than at a single geometric point. This method enables the identification of local higher discrepancies (e.g., maximum or upper-percentile errors) on quasi-conical geometries, providing a more realistic representation of potential upper-end misfits under clinical loading conditions [45–46].

Several structured-reference approaches have been proposed to improve full-arch implant scanning by increasing spatial coherence and limiting stitching drift [1,24,34,35–40]. CSS connects conventional scan bodies to reduce inter-component ‘jumps’ and support a continuous scan path [35]. Nexus IOS® introduces modular scan gauges with defined reference geometry, with both clinical and in vitro evaluations reported [36,37]. Scan Ladder and smart-flag/Apollo concepts similarly add auxiliary multi-geometry references or calibrated scan flags to facilitate recognition and reduce drift [34,38]. The present system aligns with this family of strategies but differs in implementation by integrating stabilization into a compact centripetal rotation/contact mechanism directly on MUAs, aiming to reduce inter-body spacing, scanned volume, and optical noise during acquisition.

The favourable metrological outcomes observed with the tested ISB can be largely attributed to its design and acquisition strategy. The multi-faceted dodecahedral geometry provides multiple edges and vertices that facilitate robust library matching and spatial registration, even when only partial surface information is acquired. This feature allows a substantial reduction of the scanned surface area and scanning time as the operator can scan only a portion of the scanning head. Furthermore, the centripetal rotation mechanism concentrates reference geometries toward the center of the arch. This approach reduces the overall scanned volume, limits optical noise, and mitigates cumulative stitching errors, which are known to increase with scan extension [8,13]. The solid geometry also reduces vertical voids between adjacent components, even in the presence of implant height differences, further stabilizing the acquisition geometry. However, because incomplete capture can compromise library recognition and alignment, the present partial-scan findings should be interpreted as in vitro feasibility evidence rather than a recommended clinical shortcut.

Several limitations must be acknowledged. The investigation was conducted under controlled in vitro conditions and did not reproduce intraoral variables such as saliva contamination, soft-tissue mobility, patient movement, restricted access/visibility, and clinically relevant lighting/reflection patterns; therefore, external validity is limited and the results should be interpreted as metrological proof-of-concept only. Experimental datasets were generated through library matching (CAD replacement), so outcomes primarily reflect scan-body pose estimation/transfer after matching rather than full surface-mesh fidelity. Only one IOS system and one implant configuration were evaluated, and all scans were acquired by a single expert operator, limiting generalizability and assessment of technique sensitivity. Moreover, no direct comparator (e.g., conventional scan bodies, calibrated/splinted systems, or extraoral photogrammetry) was included, and prosthetic framework fit verification was not performed; therefore, clinical implications require dedicated validation.

Future investigations should include in vivo validation, comparisons with established extraoral photogrammetry systems, and evaluations across different implant numbers and arch forms. Further research should also assess the clinical impact of the observed deviations on

framework fit and long-term prosthetic outcomes.

5. Conclusions

Based on the findings of this in vitro investigation, the following conclusions can be drawn:

- The tested ISB system demonstrated small deviations in registering implant-supported MUAs in a four-implant full-arch configuration under controlled conditions.
- The overall agreement with the reference data was high, with a global mean deviation of 0.009 mm.
- Single-MUA mean deviation was low (0.010 mm), indicating minimal site-level residual discrepancies after global registration.
- Mean translational displacement was limited (0.064 mm) and showed no evidence of a dominant directional distortion across axes.
- Rotational discrepancies were low (overall mean angular deviation 0.203°), with no significant overall site-related effect.
- Interimplant spatial fidelity showed minimal deviations of 0.003 mm.
- The acquisition workflow was efficient, with a mean scanning time of 9.0 s per scan.

Further comparative in vitro and in vivo studies are required to confirm these results, and before clinical performance claims can be made.

Funding

This research did not receive any specific grant from funding agencies in the public, commercial, or not-for-profit sectors.

CRediT authorship contribution statement

Gennaro Ruggiero: Software, Project administration, Methodology, Investigation, Formal analysis, Data curation, Conceptualization. **Roberto Sorrentino:** Formal analysis, Data curation. **Fanny Ficuciello:** Investigation, Data curation. **Lucio Lo Russo:** Methodology. **Fariba Esperouz:** Formal analysis. **Fernando Zarone:** Investigation, Formal analysis, Conceptualization.

Declaration of competing interest

The authors declare that they have no conflicts of interest.

Acknowledgments

There are no acknowledgments.

Supplementary materials

Supplementary material associated with this article can be found, in the online version, at doi:10.1016/j.jdent.2026.106623.

References

[1] A. Pozzi, L. Arcuri, P. Carosi, A. Laureti, J. Londono, H.-L. Wang, Photogrammetry versus intraoral scanning in complete-arch digital implant impression: a systematic review and meta-analysis, Clin. Implant Dent. Relat. Res. 27 (2025) e70059.
[2] M. Revilla-León, D.E. Kois, J.C. Kois, A guide for maximizing the accuracy of intraoral digital scans. Part 1: operator factors, J. Esthet. Restor. Dent. 35 (2023) 230–240.
[3] M. Revilla-León, D.E. Kois, J.C. Kois, A guide for maximizing the accuracy of intraoral digital scans. Part 2: patient factors, J. Esthet. Restor. Dent. 35 (2023) 241–249.
[4] J. Abduo, V. Bennani, N. Waddell, K. Lyons, M. Swain, Assessing the fit of implant fixed prostheses: a critical review, Int. J. Oral Maxillofac. Implants. 25 (2010) 506–515.
[5] E. Couso-Queiruga, C.A. Ramseier, V. Chappuis, S.F.M.M. Janner, D. Buser, U. Brägger, et al., Impact of marginal misfit in implant-supported fixed dental prostheses on peri-implant bone levels: A retrospective quantitative analysis, Clin. Oral Implants Res. 37 (2026) 69–78.
[6] International Organization for Standardization, ISO 5725-1:1994, Accuracy (trueness and precision) of measurement methods and results-Part 1: General principles and definitions, ISO, Geneva, 1994.
[7] International Organization for Standardization, ISO 20896-1:2019, Dentistry-Digital impression devices-Part 1: Methods for assessing accuracy, ISO, Geneva, 2019.
[8] A. Ender, A. Mehl, Accuracy of complete-arch dental impressions: a new method of measuring trueness and precision, J. Prosthet. Dent. 109 (2013) 121–128.
[9] C. Wulfman, A. Naveau, C. Rignon-Bret, Digital scanning for complete-arch implant-supported restorations: a systematic review, J. Prosthet. Dent. 124 (2020) 161–167.
[10] V. Vitai, A. Németh, E. Sólyom, L.M. Czumbel, B. Szabó, R. Fazekas, et al., Evaluation of the accuracy of intraoral scanners for complete-arch scanning: a systematic review and network meta-analysis, J. Dent. 137 (2023) 104636.
[11] A. Sallorenzo, M. Gómez-Polo, Comparative study of the accuracy of an implant intraoral scanner and that of a conventional intraoral scanner for complete-arch fixed dental prostheses, J. Prosthet. Dent. 128 (2022) 1009–1016.
[12] M. Gómez-Polo, F. Alvarez, R. Ortega, C. Gómez-Polo, A.B. Barmak, J.C. Kois, et al., Influence of the implant scan body bevel location, implant angulation and position on intraoral scanning accuracy: an in vitro study, J. Dent. 121 (2022) 104122.
[13] F. Grande, A. Mosca Balma, F. Mussano, S. Catapano, Effect of implant scan body type, intraoral scanner and scan strategy on the accuracy and scanning time of a maxillary complete-arch implant scan: an in vitro study, J. Dent. 159 (2025) 105782.
[14] A. Limones, D. Morton, A. Sallorenzo, W.-S. Lin, R. Sadid-Zadeh, K. Phasuk, et al., Impact of operator experience on intraoral digital scanning: a systematic review, meta-analysis, and meta-regression, J. Prosthet. Dent. (2025), https://doi.org/10.1016/j.prosdent.2025.09.008. S0022-3913(25)00735-8.
[15] R. Nedelcu, P. Olsson, M. Thulin, I. Nyström, A. Thor, In vivo trueness and precision of full- arch implant scans using intraoral scanners with three different acquisition protocols, J. Dent. 128 (2023) 104308.
[16] R. Lo Giudice, C. Galletti, J.P.M. Tribst, L.P. Melenchón, M. Matarese, A. Miniello, et al., In vivo analysis of intraoral scanner precision using open-source 3D software, Prosthesis 4 (2022) 554–563.
[17] M. Revilla-León, W. Att, M. Özcan, J. Rubenstein, Comparison of conventional, photogrammetry, and intraoral scanning accuracy of complete-arch implant impression procedures evaluated with a coordinate measuring machine, J. Prosthet. Dent. 125 (2021) 470–478.
[18] F. Puleio, F. Salmeri, E. Lupi, I. Urbano, R. Gasparro, S. De Vita, et al., In vivo accuracy assessment of two intraoral scanners using open-source software: a comparative full-arch pilot study, Oral 5 (2025) 97.
[19] M. Tallarico, M. Qaddomi, E. De Rosa, C. Cacciò, Y.J. Jung, S.M. Meloni, et al., Accuracy and precision of digital impression with reverse scan body prototypes and all-on-4 protocol: an in vitro research, Prosthesis 7 (2025) 36.
[20] F. Zarone, G. Ruggiero, M. Ferrari, F. Mangano, T. Joda, R. Sorrentino, Comparison of different intraoral scanning techniques on the completely edentulous maxilla: an in vitro 3-dimensional comparative analysis, J. Prosthet. Dent. 124 (2020) 762.e1–762.e8.
[21] R. Sorrentino, G. Ruggiero, R. Leone, M.I. Di Mauro, E.F. Cagidiaco, T. Joda, et al., Influence of different palatal morphologies on the accuracy of intraoral scanning of the edentulous maxilla: a three-dimensional analysis, J. Prosthodont. Res. 68 (2024) 634–642.
[22] R. Sorrentino, F. Zarone, T. Cantile, A. Mastrosimone, G. Cervino, G. Ruggiero, The use of digital tools in an interdisciplinary approach to comprehensive prosthodontic treatments, Prosthesis 6 (2024) 863–887.
[23] Y.J. Zhang, S.J. Qian, H.C. Lai, J.Y. Shi, Accuracy of photogrammetric imaging versus conventional impressions for complete-arch implant-supported fixed dental prostheses: a comparative clinical study, J. Prosthet. Dent. 130 (2023) 212–218.
[24] F.G. Mangano, H. Lerner, G. Valle, F. Biaggini, C. Mangano, A. Dybov, Trueness of extraoral photogrammetry, intraoral photogrammetry and direct intraoral scanning in the full-arch digital implant impression: a comparative in vitro study, J. Dent. 165 (2026) 106269.
[25] T. Jemt, T. Bäck, A. Petersson, Photogrammetry-an alternative to conventional impressions in implant dentistry? A clinical pilot study, Int. J. Prosthodont. 12 (1999) 363–368.
[26] H. Atalla, H. Alhelou, F. Karaduman, O. Alawawda, F. Bayindir, Comparative accuracy of photogrammetry and intraoral scanners in recordings for complete arch implant-supported prostheses: a systematic review and meta-analysis, J. Prosthet. Dent. (2025), https://doi.org/10.1016/j.prosdent.2025.10.059. S0022-3913(25)00864-9.
[27] M. Gómez-Polo, A.B. Barmak, R. Ortega, V. Rutkunas, J.C. Kois, M. Revilla-León, Accuracy, scanning time, and patient satisfaction of stereophotogrammetry systems for acquiring 3D dental implant positions: a systematic review, J. Prosthodont. 32 (2023) 208–224.
[28] G. Çakmak, H. Yilmaz, A. Treviño, A.M. Kökat, B. Yilmaz, The effect of scanner type and scan body position on the accuracy of complete-arch digital implant scans, Clin. Implant Dent. Relat. Res. 22 (2020) 533–541.
[29] M. Revilla-León, M. Gómez-Polo, M. Drone, A.B. Barmak, C. Guinot-Barona, W. Att, et al., Impact of scanning distance on the accuracy of a photogrammetry system, J. Dent. 142 (2024) 104854.

[30] M. Gómez-Polo, M. Revilla-León, P. Herranz-Seijo, J.L. Antonaya-Martín, A. B. Barmak, R. Cascos, Do ambient lighting conditions affect the accuracy of implant position capture for complete arch prostheses using intraoral photogrammetry? J. Prosthet. Dent. (2025) https://doi.org/10.1016/j.prosdent.2025.11.008. S0022-3913(25)00878-9.
[31] M. Tallarico, A.I. Lumbau, R. Scrascia, G. Demelas, F. Sanseverino, R. Amarena, et al., Feasibility of using a prosthetic-based impression template to improve the trueness and precision of a complete arch digital impression on four and six implants: an in vitro study, Materials 13 (2020) 3543.
[32] A. Paratelli, S. Vania, C. Gómez-Polo, R. Ortega, M. Revilla-León, M. Gómez-Polo, Techniques to improve the accuracy of complete arch implant intraoral digital scans: a systematic review, J. Prosthet. Dent. 129 (2023) 844–854.
[33] M. Revilla-León, M. Gómez-Polo, V. Rutkunas, P. Ntovas, J.C. Kois, Classification of complete-arch implant scanning techniques recorded by using intraoral scanners, J. Esthet. Restor. Dent. 37 (2025) 236–243.
[34] A.B. Nulty, C. Kelly, O. Ambridge, M. Ambridge, R. Ferguson, A. Hoffer, In vitro comparison of trueness and precision of an AI-driven real-time library matching protocol using irregular geometry scan bodies, Dentistry J. 13 (2025) 533.
[35] M. Imburgia, J. Kois, E. Marino, H. Lerner, F.G. Mangano, Continuous scan strategy (CSS): a novel technique to improve the accuracy of intraoral digital impressions, Eur. J. Prosthodont. Restor. Dent. 28 (2020) 128–141, https://doi.org/10.1922/EJPRD_2105Imburgia14.
[36] H. Lerner, P. Weigl, R. Sader, M. Klein, M.A. Polack, F.J. Tuminelli, Accuracy of full-arch implant scan with Nexus IOS® scan gauges versus different conventional scan bodies: an in vitro comparative study, J. Dent. 164 (2026) 106254, https://doi.org/10.1016/j.jdent.2025.106254.
[37] M. Klein, F.J. Tuminelli, A. Sallustio, G.D. Giglio, H. Lerner, R.W. Berg, et al., Full-arch restoration with the NEXUS IOS system: a retrospective clinical evaluation of 37 restorations after a one year of follow-up, J. Dent. 139 (2023) 104741, https://doi.org/10.1016/j.jdent.2023.104741.
[38] M. Tallarico, M. Qaddomi, E. De Rosa, C. Cacciò, S.M. Meloni, I. Gendviliene, et al., Effectiveness of an AI-assisted digital workflow for complete-arch implant impressions: an In vitro comparative study, Dent. J. 13 (2025) 462.
[39] M. Revilla-León, D. Ghunaim, A.B. Barmak, F.S. Afshari, Q. Fang, S. Prasad, A systematic review of the accuracy of complete arch implant scans recorded by using noncalibrated splinting or implant scan body techniques, J. Prosthet. Dent. (2025), https://doi.org/10.1016/j.prosdent.2025.11.018. S0022-3913(25)00917-5.
[40] M. Revilla-León, D. Ghunaim, A.B. Barmak, F.S. Afshari, Q. Fang, S. Prasad, Accuracy of complete arch implant scans recorded by using calibrated scanning techniques: a systematic review and meta-analysis, J. Prosthet. Dent. (2025), https://doi.org/10.1016/j.prosdent.2025.11.029. S0022-3913(25)00931-X.
[41] R. Sorrentino, G. Ruggiero, R. Leone, E.F. Cagidiaco, M.I.D. Mauro, M. Ferrari, et al., Trueness and precision of an intraoral scanner on abutments with subgingival vertical margins: an in vitro study, J. Dent. 144 (2024) 104943.
[42] M. Chruściel-Nogalska, T. Smektała, M. Tutak, K. Sporniak-Tutak, R. Olszewski, Open-source software in dentistry: a systematic review, Int. J. Technol. Assess. Health Care. 33 (2017) 487–493.
[43] R.J. Pinto, S.A. Casado, K. Chmielewski, J.M. Caramês, D.S. Marques, Accuracy of different digital acquisition methods in complete arch implant-supported prostheses: an in vitro study, J. Prosthet. Dent. 132 (2023) 172–177.
[44] Y. Ke, Y. Zhang, S. Tian, H. Chen, Y. Sun, Accuracy of digital implant impressions using a novel structured light scanning system assisted by a planar mirror in the edentulous maxilla: an in vitro study, Clin. Oral Implants Res. 35 (2023) 876–887.
[45] L. Canullo, P. Pesce, V.C.A. Caponio, R. Iacono, F.S. Luciani, C. Raffone, et al., Effect of auxiliary geometric devices on the accuracy of intraoral scans in full-arch implant-supported rehabilitations: an in vitro study, J. Dent. 145 (2024) 104979.
[46] F. Gianfreda, C. Raffone, M. Martelli, A. Pitino, V.C.A. Caponio, P. Bollero, Conventional scan body vs. scan bodies with auxiliary geometric devices: an in vitro study for edentulous full-arch implant impressions, Front. Oral Health 6 (2025) 1574149.